

Brillouin light scattering analysis of three-magnon splitting processes in yttrium iron garnet films

Christoph Mathieu,* Valeri T. Synogatch,[†] and Carl E. Patton
Department of Physics, Colorado State University, Fort Collins, Colorado 80523
 (Received 24 September 2002; published 5 March 2003)

Wave vector and frequency selective Brillouin light scattering (BLS) has been used to measure the wave vector make up for the dipole exchange spin wave (DESW) modes which are parametrically excited by propagating magnetostatic surface wave (MSSW) pulse signals in a long and narrow yttrium iron garnet film strip through three magnon splitting processes. The signal frequency f_s was 2.65 GHz, the input pulse width was 100 ns, and the in-plane applied field was 340 Oe. In addition, time and space resolved (TSR) BLS techniques were used to map the spatio-temporal propagation properties of the MSSW and DESW modes as they evolve as a result of three magnon processes. The film thicknesses were 5–10 μm . Specific data are reported for an 8.7 μm thick film. The DESW mode frequencies are at about $f_s/2$. The DESW wave vector \mathbf{k} directions form lobes at in-plane angles of 5°–15° relative to the field. The k values are in the 10^4 rad/cm range and are quantized. The frequencies and k values match those predicted from the dispersion relations and energy and momentum conservation. Specific critical powers are associated with particular k values. The TSR data show that the MSSW pulses propagate with a wedge shaped wave front and quench in such a way as to produce the ultra short 1–2 ns wide output pulses reported previously. The quench is connected with the appearance of a corresponding half frequency DESW wedge which is nearly stationary, has a response time of a few nanoseconds, and has a decay time in excess of the 100 ns MSSW pulse width.

DOI: 10.1103/PhysRevB.67.104402

PACS number(s): 75.30.Ds, 76.50.+g, 78.35.+c, 85.70.Ge

I. INTRODUCTION

Synogatch *et al.*¹ showed recently that the launch and propagation of a relatively wide high-power magnetostatic surface wave (MSSW) pulse in a thin yttrium iron garnet (YIG) film can, under certain conditions, give an ultrashort pulse at an output transducer with a width as low as 2 ns. The necessary conditions noted in Ref. 1 include one key condition: operation with an input pulse carrier frequency f_s below 3.3 GHz. This cutoff effect was taken as an indication that three magnon splitting and confluence processes were involved. Energy conservation requires that magnons involved in the splitting be close to one-half the frequency of the signal magnons, and this is possible in YIG films only below 3.3 GHz.^{2,3}

Reference 1 focused on microwave experiments. Brillouin light scattering (BLS) has now been used to demonstrate the presence of such half-frequency magnons in the films. Some preliminary results were reported in Refs. 4 and 5. The intensity of the half-frequency light scattering signals increased as the input power was increased and the response correlated well with the ultrashort pulse formation documented in Ref. 1. Through the use of wave vector selective BLS techniques, it was also possible to determine the actual wave vectors associated with the half-frequency dipole exchange spin wave (DESW) excitations. The wave numbers were precisely at the values required for energy and momentum conservation in the splitting process. Additional data by time and space resolved BLS techniques also gave flow patterns for the signals.

This paper presents the full results of the BLS investigations on the three magnon processes responsible for the short microwave pulse formation reported in Ref. 1. The results go far beyond the elucidation of the pulse shortening mechanism. To our knowledge the data given below represent the first clear and explicit demonstration of three magnon split-

ting and the experimental identification of the properties of the product magnons. The wave vector selective BLS measurements provide direct wave number and directional distributions for the product $f_s/2$ spin waves which are generated by the MSSW pulse. The time and space resolved BLS data give the temporal and spatial characteristics of the actual splitting processes as the MSSW signal couples energy into the DESW excitations.

While the data clearly show that DESW magnons are produced by the input MSSW signal through a splitting process, evidence for the reverse confluence process is more indirect. The ultrashort pulse formation process in Ref. 1 was explained by a combination of splitting to produce DESW magnons and confluence to give a broadened MSSW spectrum and a corresponding narrowing. The time and space resolved images at the end of this paper show clearly that the MSSW pulse narrowing involves more than simple decay. The correlation between the narrowing and the DESW response supports the presence of confluence as well as splitting.

II. EXPERIMENT

The microwave measurements were performed with a long and narrow YIG film strip with pulse microwave excitation from a 50 μm wide microstrip transducer at one point on the strip and detection by a second transducer 7 mm distant from the first.⁶ Typical film strips were 3 mm wide, and 20 mm long. The films were prepared by standard liquid phase epitaxy (LPE) techniques. Films with three thicknesses, 5.1 μm , 7.2 μm , and 8.7 μm , were studied. The films had low microwave loss typical of LPE YIG, with narrow ferromagnetic resonance linewidths in the range of 0.5 Oe at 10 GHz. The data below are for the 8.7 μm sample. Similar results were obtained on the other films as well.

The films were magnetized in-plane by a static field ap-

plied perpendicular to the long side of the strip. For the data below, the static field was set at a nominal value of 340 Oe. For this perpendicular field geometry, spin wave signals propagating along the strip correspond to MSSW excitations. The input pulse duty cycle was kept below 5% in order to avoid heating effects. The output pulse signals were observed and analyzed with standard microwave detection equipment, as in Ref. 6. The cw response of the transducer structure was first measured as a function of frequency to determine an optimum operating point frequency for maximum transmission. This operating point was set at $f_s = 2.65$ GHz. The corresponding MSSW wave number was about 100 rad/cm, similar to the situation in Ref. 1. For the microwave and BLS results given below, 100 ns wide input microwave pulses at frequency f_s were applied to the input transducer.

The BLS measurements were made with a multipass tandem Fabry-Pérot (TFP) interferometer similar to the system in Ref. 7. The system was used in the forward scattering wave vector selective configuration discussed in Ref. 8. The 514.5 nm wavelength linearly polarized argon ion laser light was focused by a 12 cm focal length lens onto the YIG film at normal incidence with an incident power of 10 mW. The YIG film was mounted on a stepper motor controlled translation stage in order to obtain spatial profiles of the signal over the sample. An F1.4 photographic lens with a 50 mm focal length was used to collect the directly transmitted and forward scattered light. Crossed polarizers were used to select out the magnon scattered light from the direct forward beam.

The wave vector selective forward scattering data were obtained with an aperture placed after the collection lens to define the range of the wave vectors which contribute to the scattering, as in Ref. 8. These data were collected in two ways. In method I, different sized on-axis circular apertures were placed after the collection lens. The diaphragm diameter d defines a maximum wave number k_{\max} for the detected spin waves. Data obtained as d is stepped in small increments, all for the same incident light level and measurement time, then give the wave number distribution for the scattering. For the collection lens used here, in combination with the 514.5 nm laser wavelength, one obtains a k_{\max}/d response of 1.22×10^3 rad/cm per mm and an upper limit k_{\max} value of 4×10^4 rad/cm. The diaphragm diameter was typically incremented in steps of 1 or 2 mm. In method II, data were collected with a slit-type aperture behind the collection lens. The slit selects only those scattered magnons at a well-defined in-plane propagation direction. This propagation direction will be defined in terms of the usual polar spin wave propagation angle θ_k , measured relative to a reference axis along the in-plane static field. The slit width was 1 mm.

The time and space resolved measurements utilized the time-of-flight technique described in Ref. 9. Each time a MSSW pulse is launched at the input antenna, a time counter is started. The first detected photon after this trigger then stops the counter. After many repetitions, the register of counts vs clock bin number yields a time resolved profile of the spin wave signal. At the same time, one can select the frequency of the detected magnons through the scan window settings for the TFP system in order to monitor the MSSW

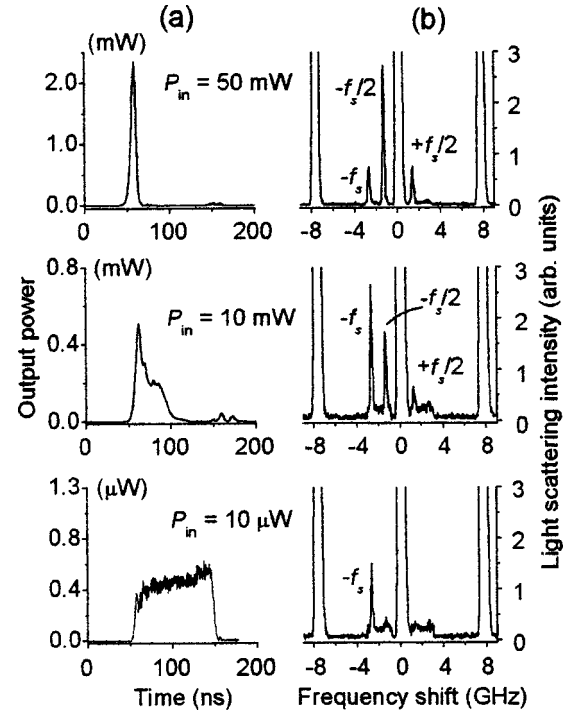


FIG. 1. (a) Output power vs time profiles for the detected MSSW pulse signals for different input peak power levels, as indicated by the P_{in} values for the three graphs. (b) Brillouin light scattering spectra corresponding to the adjacent pulse responses in (a). These results are reproduced from Ref. 4. The signal frequency was 2.65 GHz, the input pulse width was 100 ns, and the applied static field was 340 Oe. The yttrium iron garnet (YIG) film was 8.7 μ m thick.

excitations at f_s and/or the DESW excitations at $f_s/2$. The time resolution for this system is about 2 ns, and is on the order of the photon time of flight in the TFP interferometer. The space resolved data were obtained with a step size of 0.1 mm. As will be evident from the images given in Figs. 4 and 5, this 0.1×0.1 mm pixel size was more than adequate to resolve the fine structure in the propagation patterns for both the MSSW and DESW signals. The interpolated spatial resolution was below 50 μ m.

III. PULSE NARROWING AND HALF-FREQUENCY MAGNONS

Figure 1 shows microwave pulse and Brillouin light scattering data preliminary reported in Ref. 4. These data show the pulse narrowing effect discussed above and the correlations with the production of half frequency magnons. The left side panels under (a) show the microwave output pulse development as a function of the microwave input peak power P_{in} . The right side panels under (b) show the corresponding BLS spectra. These BLS measurements were done with no wave-vector selectivity and with a probe point in the middle of the YIG strip and about 1.5 mm from the launch transducer.

The data in the bottom graph in Fig. 1(a) show a low-power output pulse at $P_{in} = 10$ μ W which has the same 100 ns width as the input pulse. A distinct narrowing of the pulse

sets in as P_{in} is increased. The top graph in (a) shows an output pulse at $P_{in} = 50$ mW which has a width below 5 ns or so. Data such as these constitute the pulse narrowing effect first reported in Ref. 1. As noted in Sec. I the effect was found only for a signal frequency below 3.3 GHz, the cutoff for three magnon processes. It was this cut-off effect which first pointed to the origin of the pulse narrowing as a three magnon effect.

The BLS spectra in Fig. 1(b) document the appearance of the product $\pm f_s/2$ magnons associated with the three magnon splitting as the power is increased. Note that all of the BLS panels show strong central and ghost Rayleigh peaks at zero frequency and ± 7.5 GHz. These peaks correspond to photons at the laser frequency and the spacing corresponds to the free spectral range of the interferometer. All of the spectra also show peaks at a frequency shift of $-f_s$. These peaks correspond to the propagated MSSW signal. Extended measurement times also lead to a weak signal frequency peak at $+f_s$.

The key features of the data in Fig. 1 are (1) the emergence of the additional peaks in the BLS spectra at approximately $\pm f_s/2$ as the power level is increased, and (2) the correlation between the appearance of these peaks and the pulse narrowing effect. At the highest power levels used here with $P_{in} = 50$ mW, the BLS magnon peak at $-f_s/2$ in the upper right panel is *actually four times larger* than the MSSW signal peak at $-f_s$. These half frequency peaks constitute direct experimental evidence for the half-frequency DESW magnons produced in the splitting process.

IV. WAVE VECTOR SELECTIVE DESW ANALYSIS

The BLS evidence for $\pm f_s/2$ magnons in Fig. 1(b) represents a first step in the analysis of the product DESW spin waves in the splitting process associated with the pulse narrowing effect in Fig. 1(a). This section presents quantitative data on the wave vector makeup of the DESW signals.

First consider method I. Spectra similar to those in the top graphs of Fig. 1(b) were obtained for different diaphragm diameters and input power levels. There were two main effects. First, the scattering signal for the peak at $-f_s$ in Fig. 1(b) was independent of d , even for values below 1 mm. This response is as one would expect for the directly excited MSSW signals with wave numbers in the 100 rad/cm range. The cutoff d value here would be below 0.1 mm. The method I diaphragm could only be closed down to about 1 mm.

Second, the scattering signals for the $-f_s/2$ DESW peaks appear *only* for diaphragm diameters of about 10 mm or greater. Repeated spectra measurements of the type shown in the top two graphs of Fig. 1(b) were made as d was gradually increased. These spectra showed the sudden appearance of the $-f_s/2$ scattering peak at specific and power dependent aperture diameters. The critical d value at which these peaks appeared was found to decrease as the input power was increased. This response shows that there are different threshold power levels for the different half frequency magnon k values which satisfy the energy and momentum constraints for three magnon splitting.

The above threshold effect and the correlation between

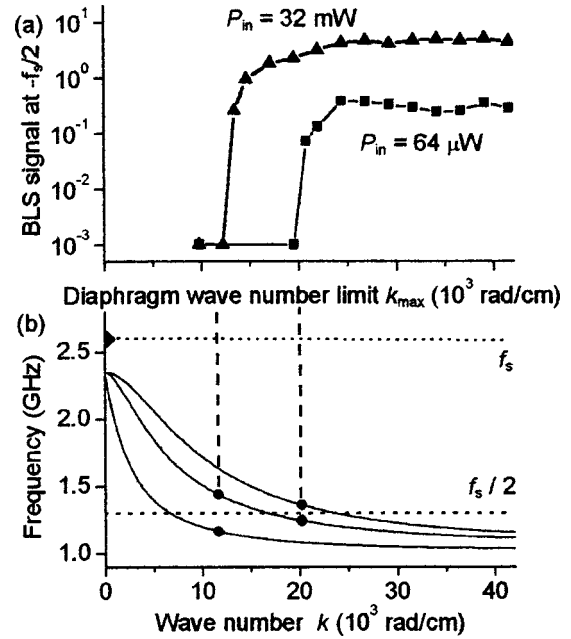


FIG. 2. (a) BLS scattering signal for the $-f_s/2$ peak as a function of the maximum allowed wave number k_{max} for two input peak power P_{in} levels, as indicated. (b) Dispersion diagrams of frequency versus wave number k for the three lowest DESW dispersion branches for film parameters that match the experiment. The solid circles, in combination with the counterpart modes at negative k values, indicate the allowed pairs of DESW modes for splitting.

the input power and the actual k distribution for the DESW signals are shown in Fig. 2. Graph (a) shows representative data on the scattering signal at $-f_s/2$ as a function of the maximum allowed wave number k_{max} . Recall from the calibration given above that k_{max}/d is 1220 rad/cm mm. The data in Fig. 2(a) were obtained from incremental increases in d in 2 mm steps, except in the vicinity of jumps where the increment was 1 mm. The actual BLS signal levels shown represent normalized intensities.

Figure 2(b) shows computed DESW dispersion curves of frequency vs wave number k . These curves are for an in-plane wave vector which is parallel to the static field and perpendicular to the MSSW propagation direction in the experiment. They were obtained from the prescription given in Ref. 10 for YIG film parameters that match the experiment. The small angle between the actual DESW wave vectors and the field axis, which is needed to conserve momentum has been ignored for these computations. The horizontal scale in (b) is set to match the scale in graph (a). The dashed horizontal line labeled f_s denotes the MSSW mode frequency and the solid point on this line at $k \approx 0$ indicates the driven MSSW mode in the experiment. The dashed line labeled $f_s/2$ indicates the half-frequency cut. The solid circles which decorate the DESW dispersion curves at k values of approximately 12 000 and 20 000 rad/cm denote those modes which combine with their counterparts at negative k to satisfy energy and momentum conservation for three magnon splitting from the MSSW mode at f_s and $k \approx 0$. Strictly speaking, the DESW modes, which satisfy momentum conservation will have wave vectors which are in plane but tilted at a small

angle away from the field direction.

As the data in Fig. 2(a) show, a gradual increase in diaphragm diameter leads to sudden onsets in the $-f_s/2$ peak intensities at specific wave number values. From the two sets of data shown, it is clear that these onset points in k are power dependent. When the input peak power is low, as for the $P_{in}=64 \mu\text{W}$ data set, the $-f_s/2$ scattering was relatively weak until the wave number exceeded about 20 000 rad/cm. When k exceeds this value, the scattering level increases abruptly by almost three orders of magnitude. When the input peak power is high, as for the $P_{in}=32 \text{ mW}$ data set, the onset of strong scattering occurred at a somewhat lower critical wave number of about 12 000 rad/cm.

The origin of the jumps in the $-f_s/2$ scattering signal at k values around 12 000 and 20 000 rad/cm in Fig. 2(a) is made clear from the dispersion curve diagrams in (b). The pairs of solid circle points on the dispersion curves equally spaced from the $f_s/2$ line represent the allowed product magnon wave numbers and frequencies which can be produced by the three magnon splitting process. The modes at $k \approx 12\,000 \text{ rad/cm}$ represent the *lowest allowed* k values for this splitting process. *No lower k modes can be excited.* The data in panel (a) show that it takes a relatively high input peak power to excite these modes. The exact minimum k points are at $11.6 \times 10^3 \text{ rad/cm}$, in very good agreement with the onset points in (a) for $P_{in}=32 \text{ mW}$. Figure 2(b) shows that the next lowest allowed k values are at about 20 000 rad/cm. The exact computed value is $20.2 \times 10^3 \text{ rad/cm}$. This k matches nicely with the lower power onset data in (a).

Reference 1 shows a more elaborate set of dispersion diagrams than shown in Fig. 2(b) with more DESW dispersion branches and mode points which extend out to much higher k values, both positive and negative. The main result from the data in Fig. 2(a) and these diagrams is that the very high k nominal half frequency modes are excited at relatively low power, and as P_{in} is increased, critical modes at lower and lower k values are also excited. It was noted above that the wave vectors for the DESW modes, which satisfy momentum conservation, are expected to lie at some small angle relative to the axis defined by the applied static field. In order to obtain a directional map of the product DESW magnons in the splitting process, additional BLS data were obtained with the method II slit diaphragm \mathbf{k} selection scheme. In this series of measurements, the scattering signal for the $-f_s/2$ peak was recorded as a function of the slit orientation angle relative to the field.

Figure 3 shows polar plots with results from these DESW angular distribution measurements at two different input peak power levels. The top graph is for a relatively low input peak power of $250 \mu\text{W}$. The bottom graph is for $P_{in}=6.3 \text{ mW}$. The horizontal $180^\circ\text{--}0^\circ$ axis denotes the field axis. The right angle arrow insert indicates the direction of the field \mathbf{H} and the orientation of the MSSW signal wave vector \mathbf{k}_s . The solid points show normalized count data. The net sample time per point was about 20 s. The detection point was about 2 mm from the launch transducer and close to the middle of the YIG strip.

The data in Fig. 3 demonstrate very clearly that the half-frequency DESW magnons which are excited in the splitting

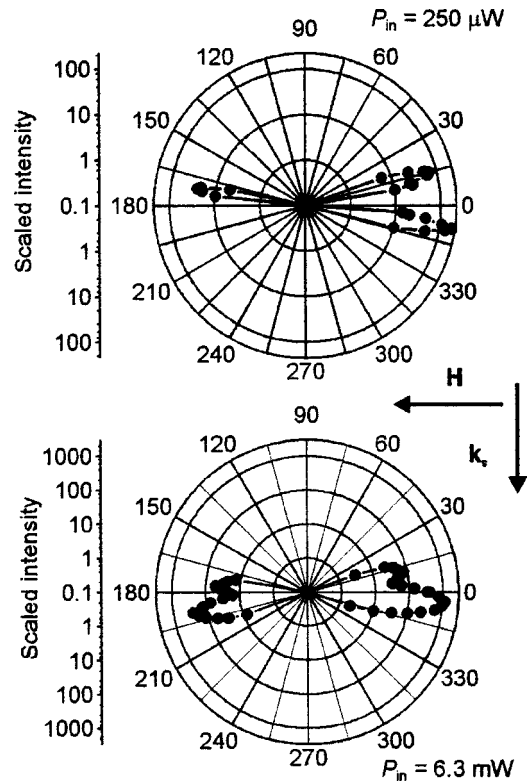


FIG. 3. Polar graphs of the BLS signal for the $-f_s/2$ DESW magnon peaks as a function of the slit diaphragm rotation angle for two different input power levels, as indicated. The right angle arrow diagram shows the directions of the static field \mathbf{H} and the MSSW wave vector \mathbf{k}_s , as indicated.

process have \mathbf{k} vectors which are constrained to lobes which are oriented at small but distinct angles relative to the field direction. The shapes and orientations of these lobes also appear to change with power. For $P_{in}=250 \mu\text{W}$, there are three strong lobes. For $P_{in}=6.3 \text{ mW}$, there appear to be four such lobes. These lobes are all directed at angles of about $5^\circ\text{--}15^\circ$ to the field axis. They are also found in four more-or-less symmetric complementary directions relative to the field axis. As the power is increased, the lobes broaden. The absence of a fourth lobe in the top panel may be due to a poorly resolved measurement for the low-power level used here. As noted above, momentum and energy conservation require the excitation of pairs of modes with \mathbf{k} vectors which project both parallel and antiparallel to the field direction. All four expected lobes appear in the high power data. Keep in mind that these data are specifically for magnon signals at or close to $-f_s/2$. Also keep in mind that the method I data have already defined the range of wave numbers which are excited at a given power.

The off axis lobe patterns in Fig. 3 are qualitatively consistent with wave vector conservation considerations. The nominal half-frequency condition which gives rise to the DESW modes in the first place was addressed above. The wave vector analysis is more complicated. Consider the situation with the two product DESW magnons with wave vectors which are nearly opposite and which make small angles θ_1 and θ_2 with the field axis. At first glance, the fact that the

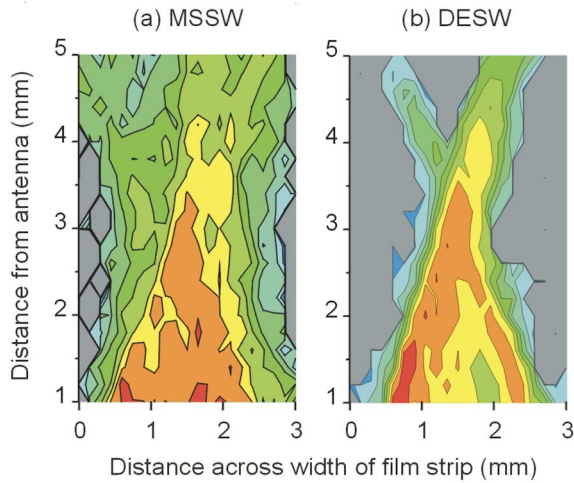


FIG. 4. (Color) The left (a) and right (b) panels show representative BLS space resolved intensity profiles for the MSSW and DESW signals, respectively. The images span the 3 mm wide YIG strips and a 4 mm propagation distance, as indicated by the horizontal and vertical scales, respectively. The pixel size for the individual point by point measurements was $0.1 \times 0.1 \text{ mm}^2$. The launch transducer is located 1 mm below the bottom edge of the panels and the propagation direction is upward. The static field was horizontal. The MSSW input peak power was 30 mW.

DESW k values are in the 10^4 -rad/cm range and the MSSW k values are in the $k_{\text{MSSW}} \approx 100$ rad/cm range suggests that these angles are very small, with $\theta_1 \approx \pi - \theta_2 \approx 0.01$ rad $\approx 0.5^\circ$. The lobe data, on the other hand, show evidence for oppositely directed DESW wave vectors with θ_1 and θ_2 in the 5° – 15° range. One can envision a situation in which the DESW magnons are oppositely directed, at $\theta_1 \approx 15^\circ$ and $\theta_2 \approx 195^\circ$, for example, but with some small deviation from a strict antiparallel configuration. A deviation in the 0.5° range allows for total wave vector conservation at the lobe angles found in the data. These relatively large observed lobe angles indicate that this is the active process here.

It is to be noted that the number of observed lobes and their power thresholds depend very strongly on the position of the observation point along the strip. It is important to keep in mind that the half-frequency DESW modes observed here are actually critical modes similar to those excited in spin-wave instability experiments.¹¹ In such experiments, the expected wave vector for the observed mode is usually obtained from a minimization procedure to determine the critical mode with the lowest threshold. Kazakov *et al.*¹² reported such a calculation for somewhat different film and operating point parameters than used here, and have obtained angles about the same as indicated in Fig. 3. Further theoretical work on such processes for thin films is needed here.

V. TIME AND SPACE RESOLVED SIGNALS

The most spectacular results from the BLS analysis of the MSSW to DESW generation process come from the space and time resolved responses for these modes. Figure 4 shows representative space resolved data. Figure 5 shows represen-

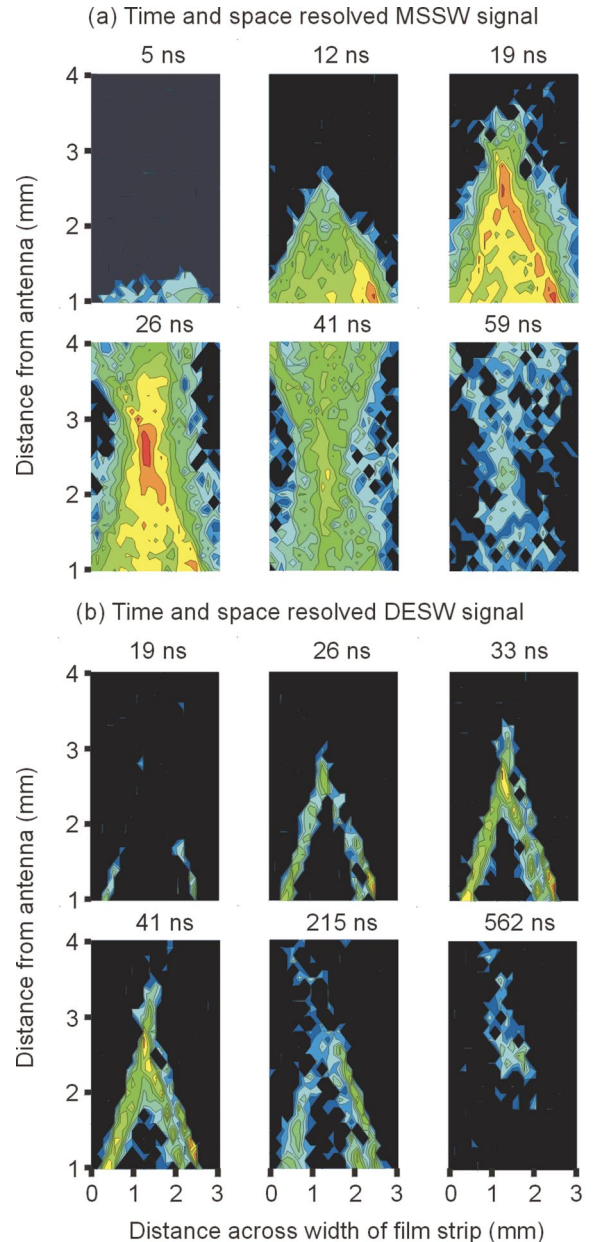


FIG. 5. (Color) The panels in (a) and (b) show time and space resolved BLS data for the MSSW pulse signal and the DESW product magnons, respectively. The images span the 3 mm wide YIG strips and a 3 mm propagation distance, as indicated by the horizontal and vertical scales, respectively. The launch transducer is located at the bottom edge of the panels and the propagation direction is upward. The numbers above each snapshot denote the time after launch of the MSSW input signal. The static field was horizontal. The MSSW input peak power was 30 mW.

tative time *and* space resolved data. In both figures, the static field \mathbf{H} is horizontal and the MSSW wave vector \mathbf{k}_s is directed upward. All data were obtained with no wave vector selective diaphragms in the collection optics. All wave vectors within the range of the forward scattering collection optics were detected. The static field and the MSSW signal frequency and pulse width for both sets of data were the same as for the results given above. Recall that the spatial

scans were for a pixel size of $0.1 \times 0.1 \text{ mm}^2$.

In Fig. 4, the left and right panels show spatially resolved power profiles for the MSSW signal at $-f_s$ and the DESW signal at $-f_s/2$, respectively. For a given profile, every pixel was measured for the same number of BLS scans, typically 50–100. There was no time selection for these data. The panels show the power profiles for the MSSW pulse propagation and DESW signal generation over the full lifetime for the signals over the film area shown. The input MSSW pulse peak power was about 30 mW. In the panels, the horizontal scale spans the 3-mm width of the YIG film and the vertical axis maps the range between 1 and 5 mm along the YIG strip from the launch transducer below the bottom edge for each image.

In Fig. 5, the series of panels under (a) and (b) are for the MSSW and the DESW signals, respectively. The horizontal span is over the 3 mm width of the YIG strip, as in Fig. 4, but the vertical axis maps only the range between 1 and 4 mm from the launch antenna at the bottom edge of each panel. The absolute time values on top of each panel in Fig. 5 indicate the time difference in nanoseconds upon launch of the MSSW input signal. The time frames extend only to about 50 ns after launch for the MSSW snapshots in (a) and to about 550 ns after launch for the DESW snapshots in (b). The spatial pixel size is the same as before. Each pixel was measured for the same number of BLS scans, typically 50.

The BLS intensity profiles in Fig. 4 show the direct spatial correlation between the MSSW and DESW excitations over the film. Perhaps the most interesting features here are in the focused energy profile for the MSSW signal in (a) and the focused cross pattern which is in evidence in (b). Keep in mind that the profiles in (a) and (b) are for a factor of 2 difference in frequency, completely different types of spin wave excitations, and completely different wave vectors. These data show very clearly the spatial correlation between the input signal MSSW magnons and the product DESW magnons. At least over the range of wave numbers accessible by the forward scattering BLS technique, the product DESW magnon profile does not extend significantly beyond the regions where there is a strong MSSW response. The intensity profile in Fig. 4 is consistent with the microwave data in Ref. 1, in that the apex in both intensity wedges is at about 3 mm from the input transducer. This point coincides with the position of highest microwave output peak power noted in Ref. 1.

The time and space resolved data in Fig. 5 yield additional results on the signal and product magnons. Consider first the MSSW response in (a). The top three panels in (a) show the same focused triangular shaped wave front for the leading edge of the MSSW pulses evident from Fig. 4. After about 20 ns, however, this triangular wave front evolves into a more or less uniform hourglass shape, as in the panel at 41 ns, and then the signal level rapidly decays, as in the last panel for 59 ns.

Keep in mind that the vertical viewing region in Fig. 5 is only 3 mm in length, not the full 7-mm distance between transducers. The input peak power was 30 mW, well below the 50 mW level needed for the extreme pulse narrowing in Fig. 1(a). The data in Fig. 5(a) suggest a pulse narrowing at

the 3 mm propagation point to some value greater than 15 ns (41–26) and less than 33 ns (59–26). These data show, quite spectacularly, how the MSSW signal initially propagates and then simply vanishes about 50 ns after launch. Note that even for the last panel at 59 ns, approximately 60 ns after launch, the input microwave power still appears in the input transducer. Even with this input power, however, the actual MSSW signal in the film at the output transducer has self-limited and is essentially zero.

The panels in (b) reveal additional features of the DESW production which are also rather spectacular. Note that the time steps for the panels in (b) span a much greater range than in (a). Taken as a whole, the panels in (b) show the same wedge shaped response as in (a), but with three important differences. One obvious difference is that the DESW wedge takes about 5–10 ns to form. The MSSW wedge is fully resolved in the 19 ns panel in (a), while the DESW wedge takes shape in the 33 ns panel in (b). It is clear that this formation is driven by the power in the MSSW drive signal. From the original pulse narrowing effect illustrated in Fig. 1, one can infer that the DESW formation time is an inverse function of the peak input power. Note that for a typical spin wave line width in the 0.5 Oe range, one has an actual relaxation time of about 200–300 ns. This time is consistent with the decay of the DESW signals. The formation process, driven by the power level of the MSSW signal, is much faster.

A second difference is that the DESW wedge appears to be almost stationary rather than propagating. All six panels in (b) show about the same topology. At 19 ns, one sees the semblance of the wedge taking shape, and by 33 ns, it is fully visible. At 41, 215, and 562 ns, the wedge fades. All six wedge images, however, are at about the same place in the film. This topology is somewhat surprising. It seems that the DESW wedge is “nucleated” when the propagating wedge shaped MSSW wave front reaches some critical amplitude. Once nucleated, these DESW wedge power profiles over the film remain more or less fixed in position.

There are two things to keep in mind with regard to these “stationary” DESW signals. First, note from Fig. 2 that the slopes of the dispersion curves at the solid circle mode points are rather small. These slopes correspond to group velocities which are in the 10^5 cm/s range, an order of magnitude or more smaller than typical MSSW group velocities. Second, note also that the Fig. 3 data show that the actual DESW signals consist of paired, oppositely directed wave vectors. This suggests that the DESW magnons may consist of standing modes. The data here support this suggestion rather clearly.

A final difference between the wedge signals in (a) and (b) is that the standing wave DESW wedges appear to be hollow. The MSSW wedge at 19 ns is a filled wedge and the strong signal region is inside the wedge. The DESW wedge power profiles all have strong signals only at the perimeter, with essentially nothing in the middle.

There is an additional point of contrast between the MSSW and DESW signals. The MSSW signal level as a function of time gives only a single maximum over the time range shown, independent of the spatial probe point. In con-

trast, one can see up to three peaks of different intensities and at different times for the DESW excitations. This observation provides further corroboration for the existence of a number of parametrically excited DESW modes. Recall that two of these modes have been identified explicitly from the wave vector selective measurement results in Fig. 2.

The responses shown in Fig. 5 clearly demonstrate three magnon splitting. Do the data also show confluence? From elementary transition probability and scattering cross-section arguments, it is clear that the splitting process must be accompanied by a reverse confluence process. As discussed in Ref. 1, the frequency spread in the DESW magnons translates into a frequency spread for the back reaction MSSW magnons of about 1 GHz. The pulse narrowing in the top graph of Fig. 1(a) is attributed to this spread spectrum of confluence-produced signals. Can one actually discern confluence from Fig. 5? The answer to the confluence question is not completely obvious from the data. The spatio-temporal MSSW response is clearly complex. The filled MSSW wedge propagates as the hollow DESW wedge is established. But in the frames from 26 to 59 ns for the MSSW profiles in Fig. 5(a), one sees a more-or-less hourglass shape energy profile take shape and then simply disintegrate. This disintegration occurs as the DESW wedges fade. This response does imply some kind of back interaction. Otherwise, one would expect the MSSW wedge simply to fade due to normal decay. Confluence of the sort proposed in Ref. 1 is the most logical option for this reverse effect.

VI. SUMMARY AND CONCLUSIONS

The above results show that Brillouin light scattering is the method of choice to study magnon processes in yttrium iron garnet thin films. The frequency and wave vector selectivity capabilities of the BLS technique are seen to give a direct and unambiguous correlation between the ultra short microwave pulse formation and three-magnon processes. As the input MSSW pulses propagate at high power and the pulse shortening sets in, the product half-frequency magnons are shown to be dipole exchange spin wave (DESW) excitations with large wave vectors in the 10^4 rad/cm range. Further wave vector selective measurements show that the in-plane DESW wave vectors are limited to angular

lobes oriented at angles of about 5° – 15° relative to the field axis.

The time and space resolved data also yield new insights into the dynamics of the splitting process. While the spatially resolved intensity distributions for the two types of spin waves match quite closely, the time profiles for these excitations are very different. The MSSW magnons propagate as one continuous pulse. The shortening appears to occur as the DESW magnon signal is produced. The DESW magnons, once produced, seem to be almost stationary, with group velocities which are at least five times smaller than those for the MSSW signal.

The significance of this work goes beyond the elucidation of one particular nonlinear spin-wave generation process in a YIG film. This work demonstrates that time and spatially resolved, wave vector selective Brillouin light scattering is a powerful and versatile tool for the investigation of high-frequency magnetization dynamics in magnetic thin films.

Note added in proof. Professor G. A. Melkov, Kiev Taras Shevchenko National University, Ukraine, has kindly pointed out three important references. Pulse narrowing due to nonlinear spin wave interactions was observed by Sansalone and Spencer,¹³ and the related limiter effect was discussed by Stern.¹⁴ Three magnon splitting for magnetostatic surface waves at high power was reported in Ref. 15, along with measurements of the small frequency shifts of the spin waves from $f_s/2$.

ACKNOWLEDGMENTS

This work was supported in part by the U.S. Army Research Office, Grants DAAG55-98-1-0430 and DAAD19-02-1-0197, the National Science Foundation, Grants DMR-9801649 and DMR-0108797, and the North Atlantic Treaty Organization (NATO), Grant Nos. HTECH.LG.970538 and PST.CLG.978096. Professor Boris A. Kalinikos, St. Petersburg Electrotechnical University, St. Petersburg, Russia and Professor Andrei N. Slavin, Oakland University, Rochester, Michigan are acknowledged for helpful discussions. The YIG films used in this work were provided by Professor Yuri K. Fetisov, Moscow Institute of Radio Engineering, Electronics, and Automation (MIREA), Moscow, Russia and by Professor Kalinikos.

*Present address: Seagate Recording Heads Division, 7801 Computer Avenue South, Bloomington, MN 55435. Email address: christoph.mathieu@seagate.com

†Present address: Hitachi Global Storage Technologies, 5600 Cottle Road, San Jose, CA 95193. Email address: synogach@us.ibm.com

¹V. T. Synogach, Y. K. Fetisov, C. Mathieu, and C. E. Patton, *Phys. Rev. Lett.* **85**, 2184 (2000).

²M. Sparks, *Ferromagnetic Relaxation Theory* (McGraw Hill, New York, 1964).

³A. M. Mednikov, *Fiz. Tverd. Tela (Leningrad)* **23**, 242 (1981) [*Sov. Phys. Solid State* **23**, 136 (1981)].

⁴C. Mathieu, V. T. Synogach, and C. E. Patton, *Ferrites: Proceedings of the Eighth International Conference on Ferrites (ICF8)*, Kyoto and Tokyo, Japan, 2000 (Japan Society of Powder Metallurgy, Kyoto, 2001), pp. 873–875.

⁵C. Mathieu, V. T. Synogach, and C. E. Patton, *8th MMM-Intermag Conference, San Antonio, Texas, January 7–11, 2001*, Abstract AF-09.

⁶N. G. Kovshikov, B. A. Kalinikos, C. E. Patton, E. S. Wright, and J. M. Nash, *Phys. Rev. B* **54**, 15 210 (1996).

⁷B. Hillebrands, *Rev. Sci. Instrum.* **70**, 1589 (1999).

⁸G. Srinivasan, C. E. Patton, and P. R. Emtage, *J. Appl. Phys.* **61**,

- 2318 (1987).
- ⁹O. Büttner, M. Bauer, A. Rueff, S. O. Demokritov, B. Hillebrands, A. N. Slavin, M. P. Kostylev, and B. A. Kalinikos, *Ultramicroscopy* **38**, 443 (2000).
- ¹⁰B. A. Kalinikos, *Sov. Phys. J.* **24**, 718 (1981).
- ¹¹M. Chen and E. E. Patton, in *Nonlinear Phenomena and Chaos in Magnetic Materials*, edited by P. E. Wigen (World Scientific, Singapore, 1994).
- ¹²G. T. Kazakov, A. V. Kozhevnikov, and Y. A. Filimonov, *Fiz. Tverd. Tela (St. Petersburg)* **38**, 330 (1997) [*Phys. Solid State* **39**, 288 (1997)].
- ¹³F. J. Sansalone and E. G. Spencer, *IRE Trans. Microwave Theory Tech.* **9**, 272 (1961).
- ¹⁴E. Stern, *J. Appl. Phys.* **32**, 315S (1961).
- ¹⁵G. A. Melkov and S. V. Sholom, *Zh. Eksp. Teor. Fiz.* **96**, 712 (1989) [*Sov. Phys. JETP* **69**, 403 (1989)].